ภาคผนวก

ภาคผนวก ก
ภาพถ่ายโครงสร้างจุลภาคก่อนกัดกรดและหลังกัดกรด

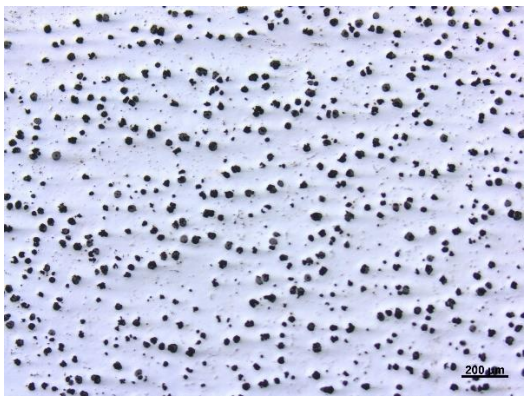

ความหนา 4 มิลลิเมตร

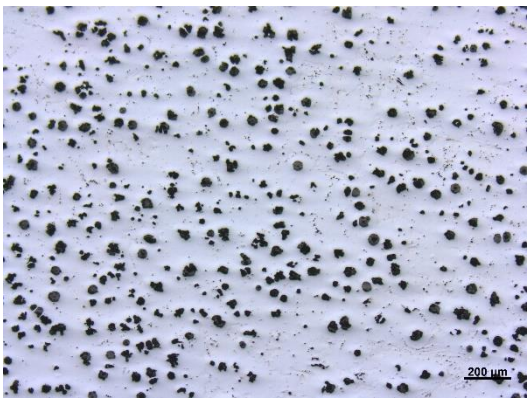

ความหนา 9 มิลลิเมตร

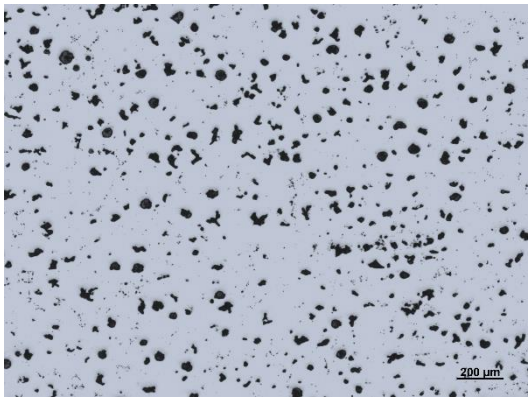

ความหนา 16 มิลลิเมตร

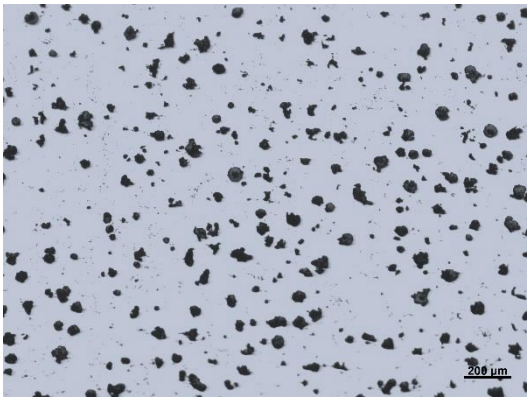

ความหนา 25 มิลลิเมตร

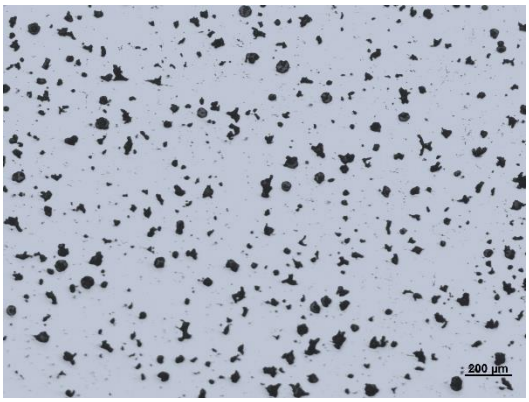

ความหนา 36 มิลลิเมตร

รูปที่ ก.1 โครงสร้างจุลภาคของเหล็กหล่อเหนียวที่มีบิสมัท 0.0001% และความหนาตั้งแต่ 4-36 มิลลิเมตร (ก่อนกัดกรด)

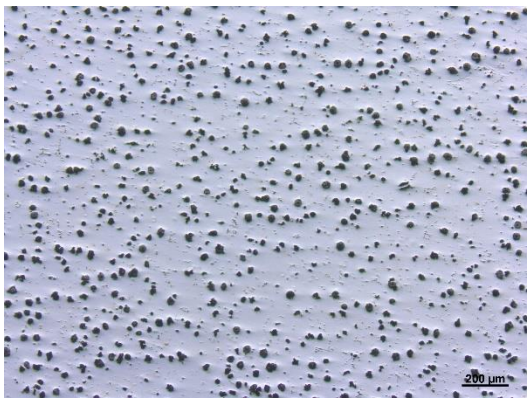

ความหนา 4 มิลลิเมตร

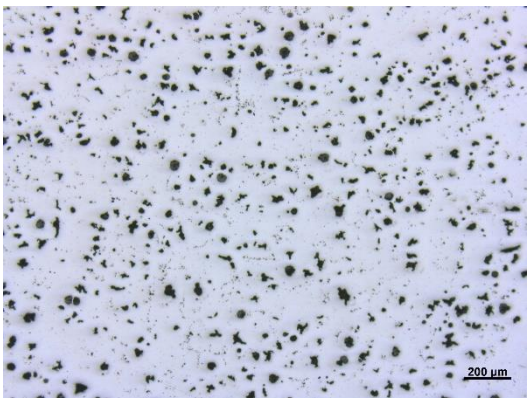

ความหนา 9 มิลลิเมตร

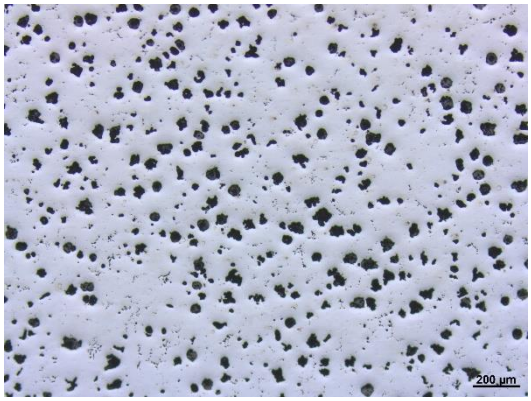

ความหนา 16 มิลลิเมตร

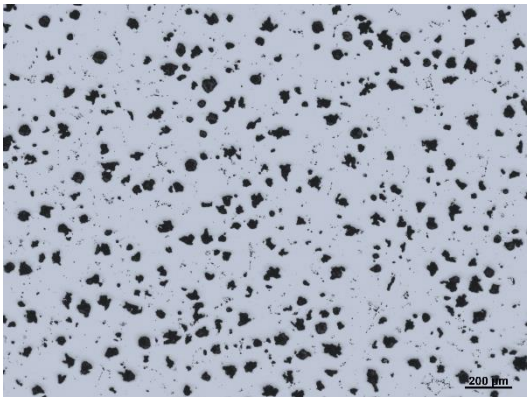

ความหนา 25 มิลลิเมตร

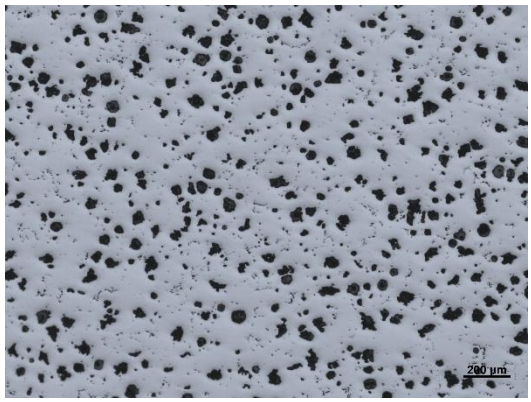

ความหนา 36 มิลลิเมตร

รูปที่ ก.2 โครงสร้างจุลภาคของเหล็กหล่อเหนียวที่มีบิสมัท 0.003% และความหนาตั้งแต่ 4-36 มิลลิเมตร (ก่อนกัดกรด)

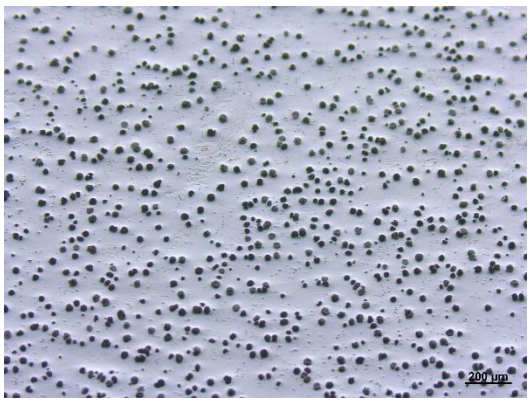

ความหนา 4 มิลลิเมตร

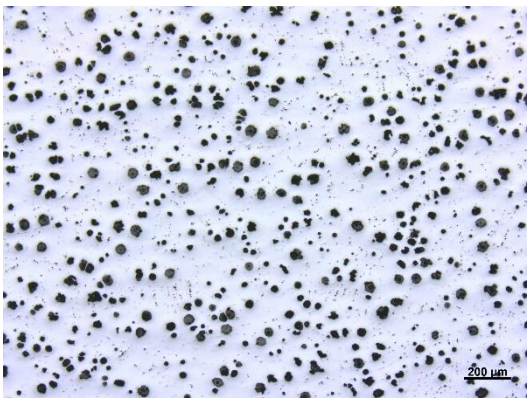

ความหนา 9 มิลลิเมตร

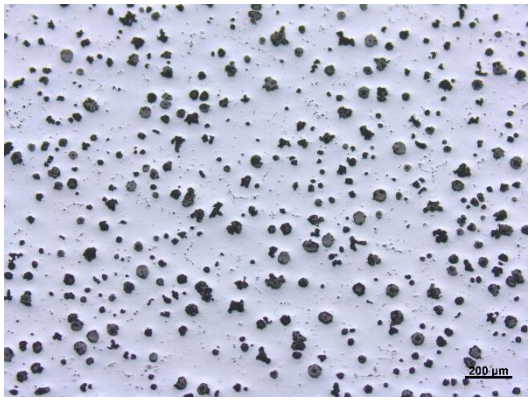

ความหนา 16 มิลลิเมตร

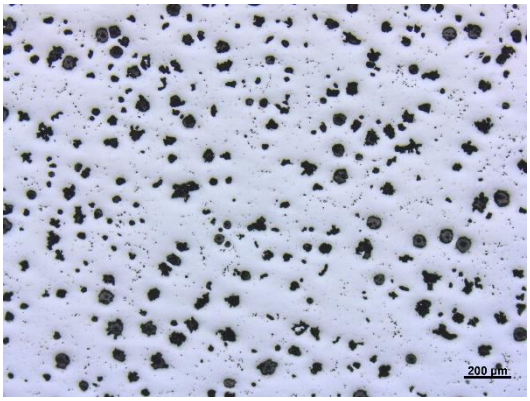

ความหนา 25 มิลลิเมตร

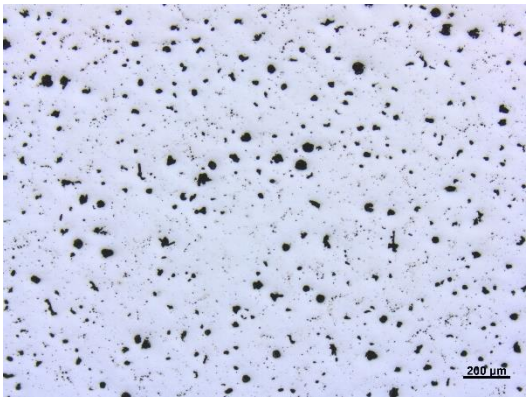

ความหนา 36 มิลลิเมตร

รูปที่ ก.3 โครงสร้างจุลภาคของเหล็กหล่อเหนียวที่มีบิสมัท 0.005% และความหนาตั้งแต่ 4-36 มิลลิเมตร (ก่อนกัดกรด)

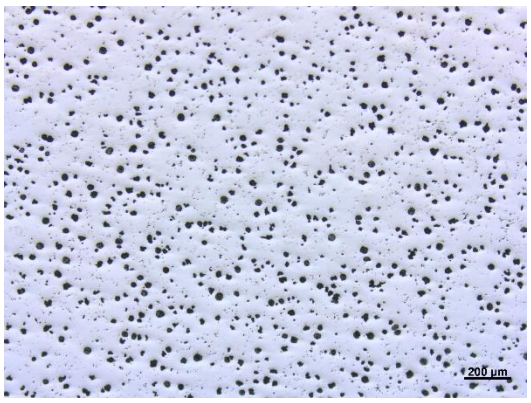

ความหนา 4 มิลลิเมตร

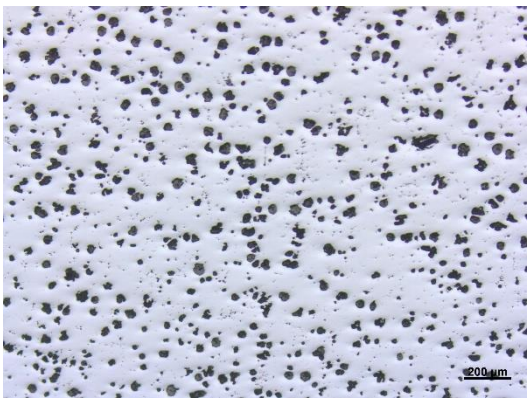

ความหนา 9 มิลลิเมตร

ความหนา 16 มิลลิเมตร

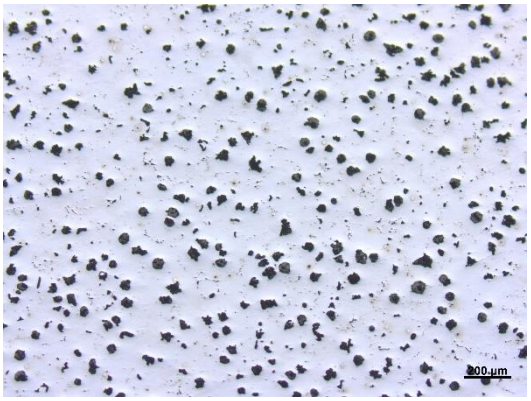

ความหนา 25 มิลลิเมตร

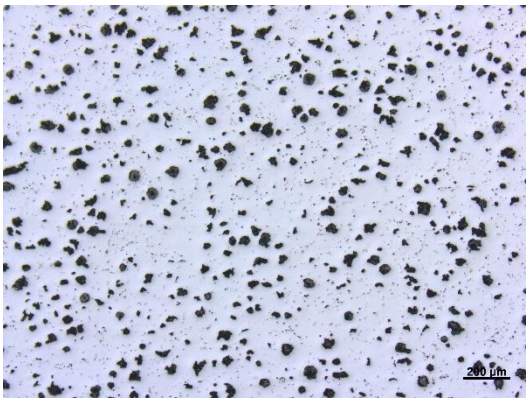

ความหนา 36 มิลลิเมตร

รูปที่ ก.4 โครงสร้างจุลภาคของเหล็กหล่อเหนียวที่มีบิสมัท 0.007% และความหนาตั้งแต่ 4-36 มิลลิเมตร (ก่อนกัดกรด)

ความหนา 4 มิลลิเมตร

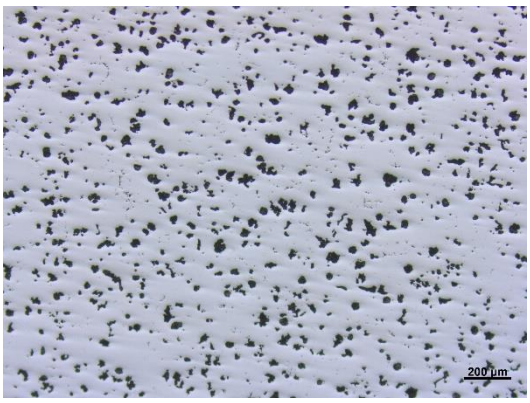

ความหนา 9 มิลลิเมตร

ความหนา 16 มิลลิเมตร

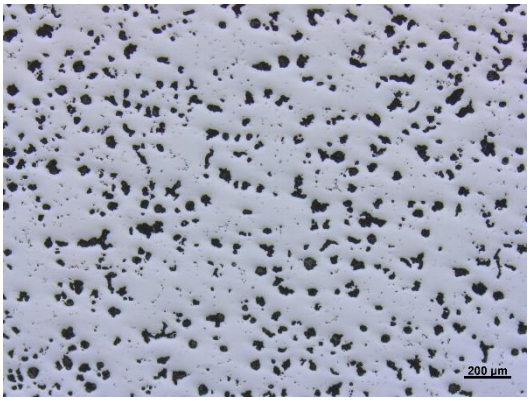

ความหนา 25 มิลลิเมตร

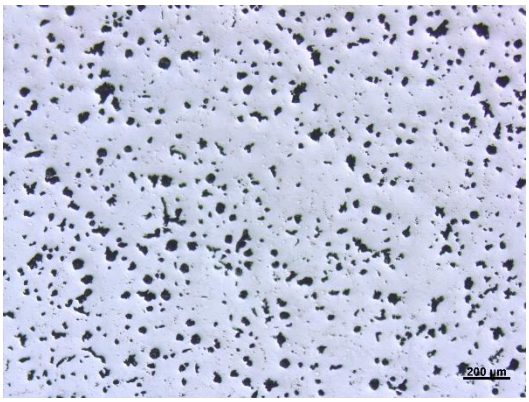

ความหนา 36 มิลลิเมตร

รูปที่ ก.5 โครงสร้างจุลภาคของเหล็กหล่อเหนียวที่มีบิสมัท 0.010% และความหนาตั้งแต่ 4-36 มิลลิเมตร (ก่อนกัดกรด)

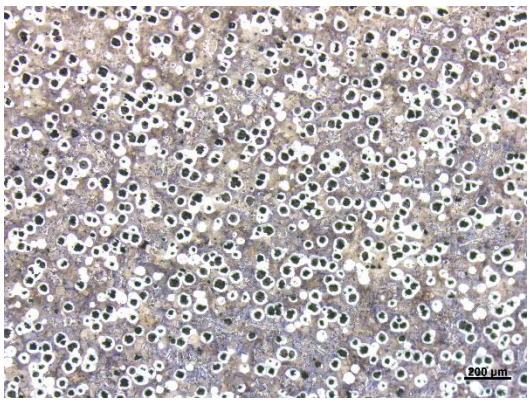

ความหนา 4 มิลลิเมตร

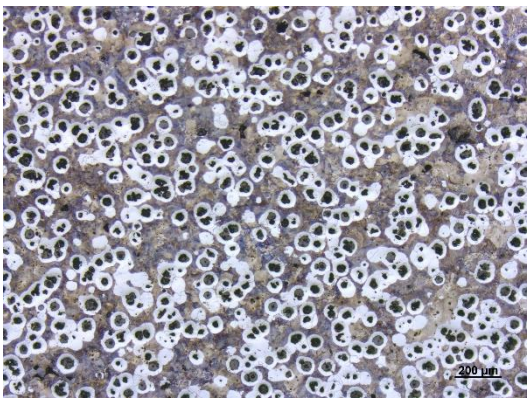

ความหนา 9 มิลลิเมตร

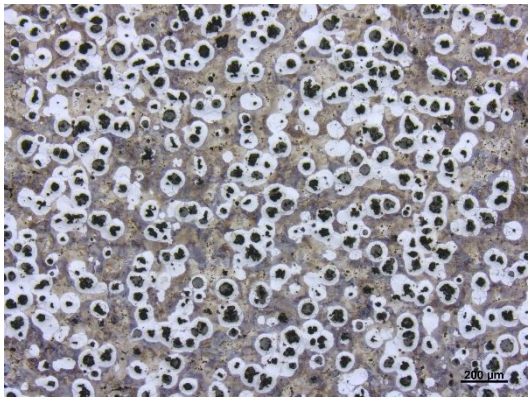

ความหนา 16 มิลลิเมตร

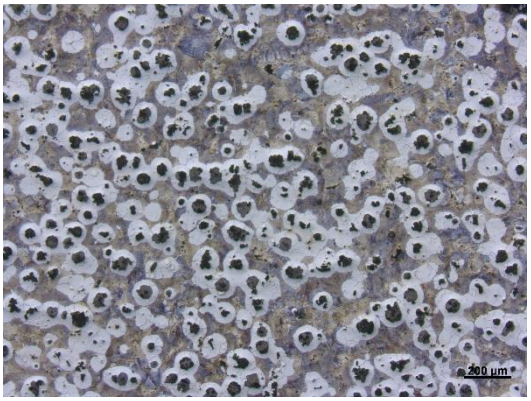

ความหนา 25 มิลลิเมตร

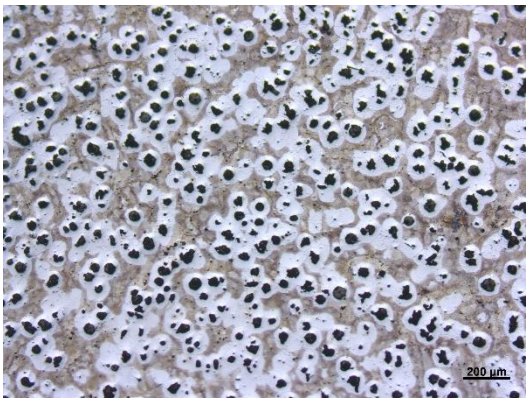

ความหนา 36 มิลลิเมตร

รูปที่ ก.6 โครงสร้างจุลภาคของเหล็กหล่อเหนียวที่มีบิสมัท 0.0001% และความหนาตั้งแต่ 4-36 มิลลิเมตร (หลังกัดกรด)

ความหนา 4 มิลลิเมตร

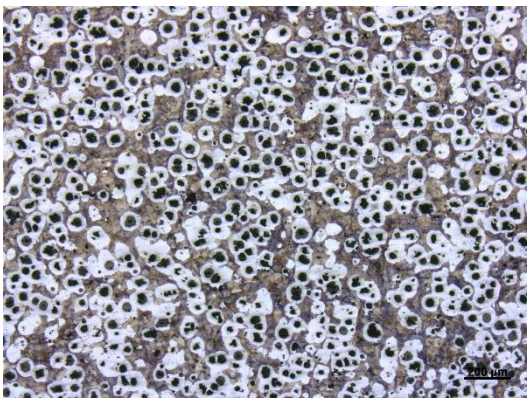

ความหนา 9 มิลลิเมตร

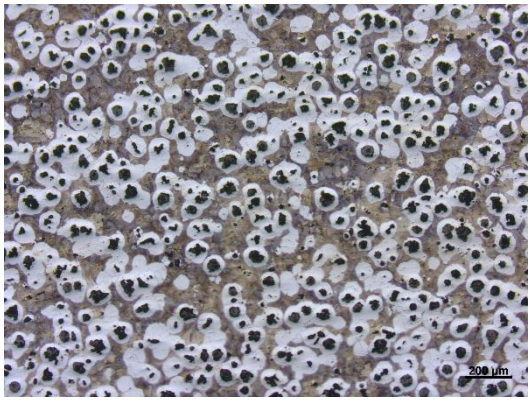

ความหนา 16 มิลลิเมตร

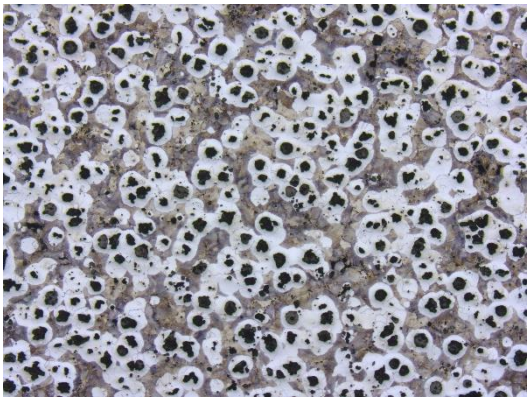

ความหนา 25 มิลลิเมตร

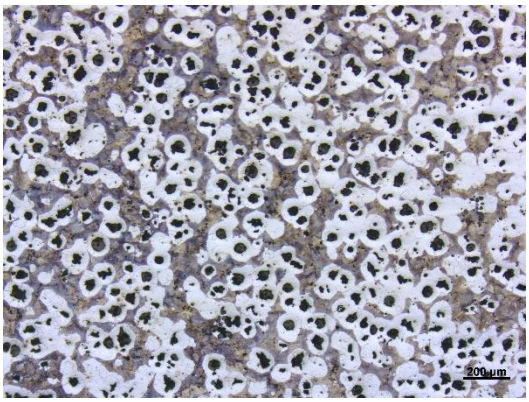

ความหนา 36 มิลลิเมตร

รูปที่ ก.7 โครงสร้างจุลภาคของเหล็กหล่อเหนียวที่มีบิสมัท 0.003% และความหนาตั้งแต่ 4-36 มิลลิเมตร (หลังกัดกรด)

ความหนา 4 มิลลิเมตร

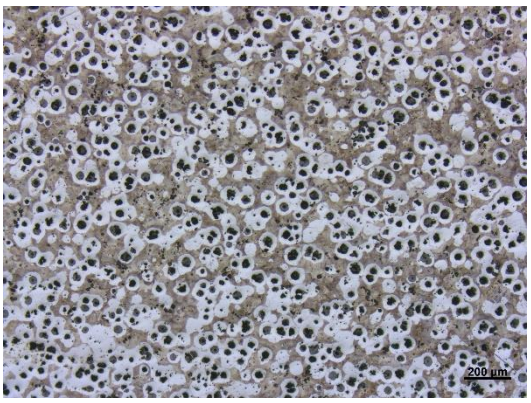

ความหนา 9 มิลลิเมตร

ความหนา 16 มิลลิเมตร

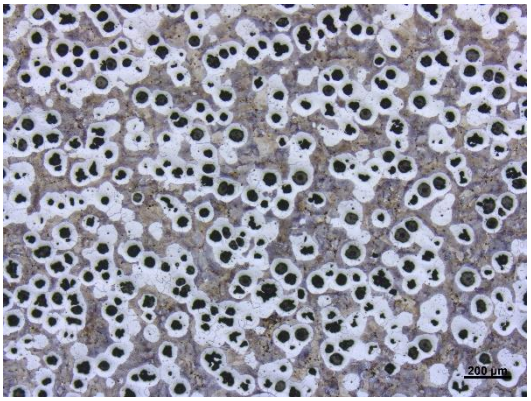

ความหนา 25 มิลลิเมตร

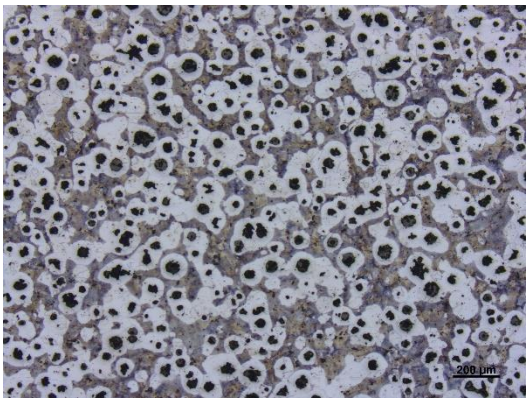

ความหนา 36 มิลลิเมตร

รูปที่ ก.8 โครงสร้างจุลภาคของเหล็กหล่อเหนียวที่มีบิสมัท 0.005% และความหนาตั้งแต่ 4-36 มิลลิเมตร (หลังกัดกรด)

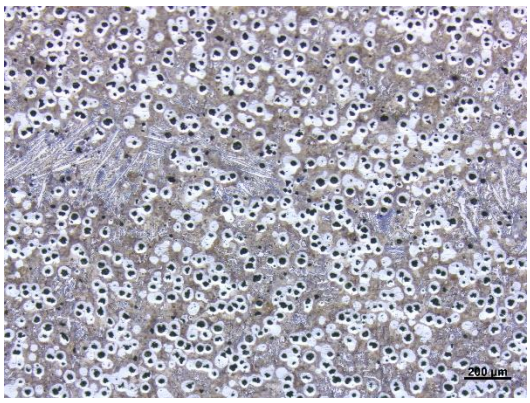

ความหนา 4 มิลลิเมตร

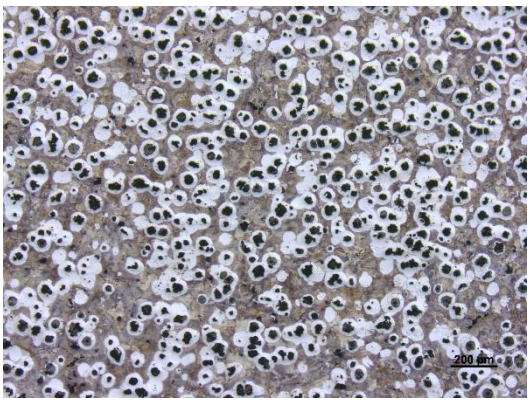

ความหนา 9 มิลลิเมตร

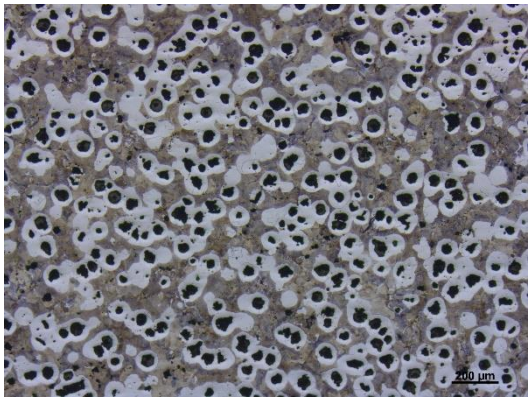

ความหนา 16 มิลลิเมตร

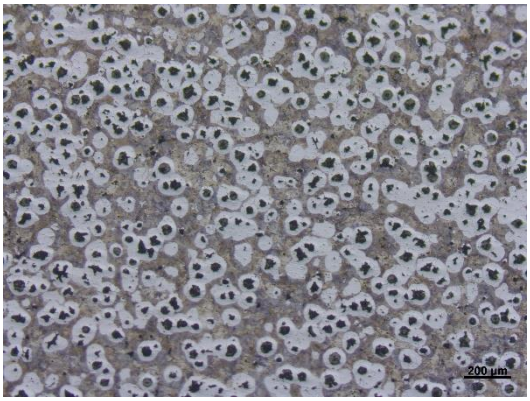

ความหนา 25 มิลลิเมตร

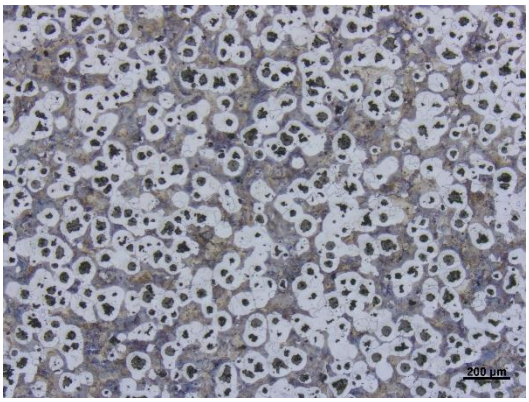

ความหนา 36 มิลลิเมตร

รูปที่ ก.9 โครงสร้างจุลภาคของเหล็กหล่อเหนียวที่มีบิสมัท 0.007% และความหนาตั้งแต่ 4-36 มิลลิเมตร (หลังกัดกรด)

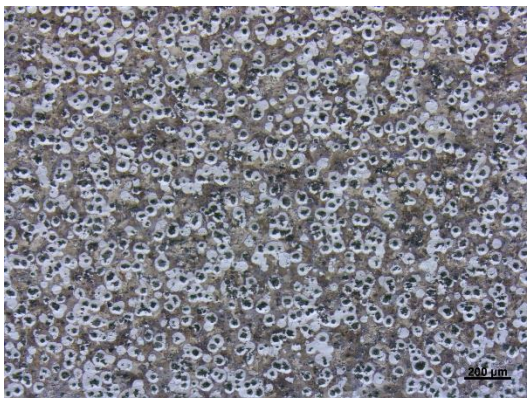

ความหนา 4 มิลลิเมตร

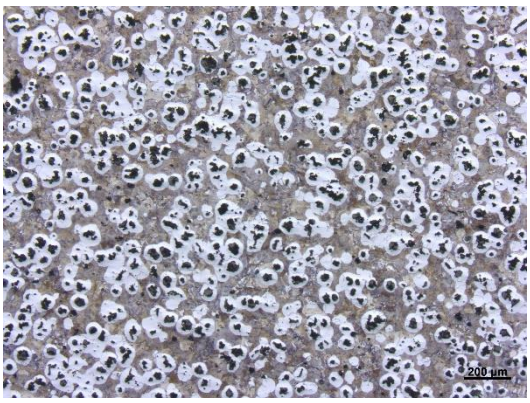

ความหนา 9 มิลลิเมตร

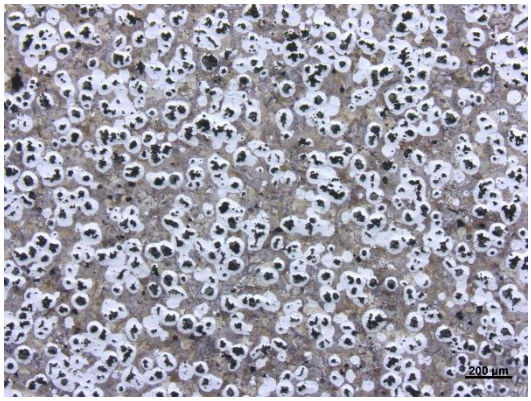

ความหนา 16 มิลลิเมตร

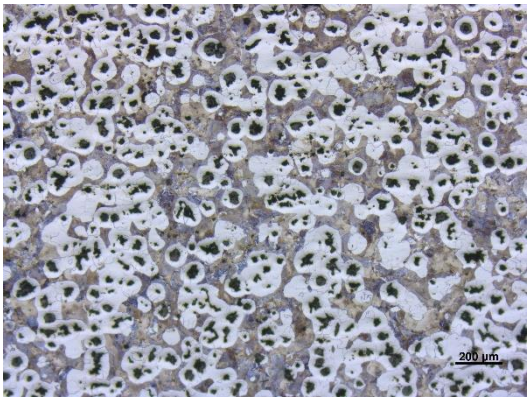

ความหนา 25 มิลลิเมตร

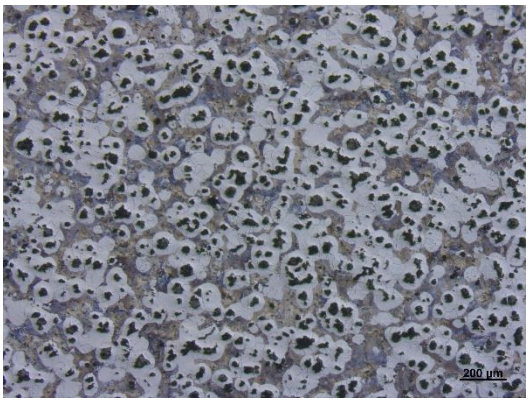

ความหนา 36 มิลลิเมตร

รูปที่ ก.10 โครงสร้างจุลภาคของเหล็กหล่อเหนียวที่มีบิสมัท 0.010% และความหนาตั้งแต่ 4-36 มิลลิเมตร (หลังกัดกรด)

ภาคผนวก ข
ผลทดสอบสมบัติเชิงกล

ตารางที่ ข.1 ค่าความแข็งแรงของจุดคราก (Yield Strength, YS) และค่าความต้านทานแรงดึงสูงสุด (Ultimate Tensile Strength, UTS) ของเหล็กหล่อเหนียวที่มีบิสมัทตั้งแต่ 0 – 0.01%

Sample	NO.	Yield Strength (MPa)	Tensile Strength (MPa)
0.000 %Bi	1	460.7	562.3
	2	409.7	411.3
	3	402.6	402.6
	เฉลี่ย	**424.3**	**458.7**
0.003 %Bi	1	436.7	468.6
	2	486.7	570.9
	3	485.3	534.4
	เฉลี่ย	**469.6**	**524.6**
0.005 %Bi	1	454.8	584.8
	2	470.3	588.9
	3	491.0	507.0
	เฉลี่ย	**472.0**	**560.2**
0.007 %Bi	1	455.2	538.8
	2	423.5	579.6
	3	456.7	521.3
	เฉลี่ย	**445.1**	**546.6**
0.010 %Bi	1	439.8	456.9
	2	414.6	537.0
	3	404.4	524.5
	เฉลี่ย	**419.6**	**506.1**

ตารางที่ ข.2 ค่าความแข็งของเหล็กหล่อเหนียวที่มีบิสมัทตั้งแต่ 0 – 0.01%

%Bi	ความหนา	ทดสอบความแข็ง (รอบ)					
	(mm)	1	2	3	4	5	เฉลี่ย
0.000 %Bi	4	110.8	110.3	109.3	108.9	109.3	109.72
	9	98.2	99.9	98.2	98.1	97.0	98.28
	16	92.5	95.1	95.3	93.7	92.9	93.90
	25	94.0	93.1	93.7	94.7	92.9	93.68
	36	88.7	90.0	89.5	90.0	88.1	89.26
0.003 %Bi	4	106.4	105.5	105.8	107.3	110.6	107.12
	9	93.2	94.8	94.6	93.6	92.5	93.74
	16	92.2	93.2	94.1	92.8	93.3	93.12
	25	90.6	90.6	91.0	91.0	90.6	90.76
	36	92.4	89.9	89.8	88.2	89.7	90.00
0.005 %Bi	4	105.5	104.0	104.1	104.9	106.2	104.94
	9	96.8	98.9	97.3	96.1	98.1	97.44
	16	93.0	93.7	95.3	94.7	94.5	94.24
	25	92.2	94.3	94.0	94.2	91.4	93.22
	36	91.5	93.5	92.0	92.9	92.9	92.56
0.007 %Bi	4	105.0	101.3	99.0	97.0	99.1	100.28
	9	93.6	93.1	93.7	93.1	91.6	93.02
	16	92.7	91.7	92.8	91.0	91.8	92.00
	25	89.5	92.0	92.0	93.0	91.6	91.62
	36	83.9	85.7	85.4	88.0	88.7	86.34
0.010 %Bi	4	95.1	94.5	94.2	97.0	97.1	95.58
	9	93.0	92.6	94.3	95.3	93.2	93.68
	16	90.6	93.0	93.0	94.6	90.6	92.36
	25	87.3	87.6	90.8	91.3	89.8	89.36
	36	86.6	88.7	89.3	88.3	87.1	88.00

ภาคผนวก ค
การหาค่าคาร์บอนสมมูล (Carbon Equivalent)

การหาค่าคาร์บอนสมมูล (Carbon Equivalent)

$$CE = \%C + \left(\frac{\%Si + \%P}{3} \right)$$

โดย %C คือ ร้อยละโดยน้ำหนักของธาตุคาร์บอนที่เจืออยู่ในเหล็กหล่อ

%Si คือ ร้อยละโดยน้ำหนักของธาตุซิลิคอนที่เจืออยู่ในเหล็กหล่อ

%P คือ ร้อยละโดยน้ำหนักของธาตุฟอสฟอรัสที่เจืออยู่ในเหล็กหล่อ

ภาคผนวก ง
บทความวิชาการที่ได้รับการตีพิมพ์เผยแพร่ในระหว่างการศึกษา

รายชื่อบทความวิชาการที่ได้รับการตีพิมพ์เผยแพร่

S. Boonmee*, **W. Waenthongkam**, K. Worakhut (2024). **Effect of Bismuth on Microstructure and Properties of Ductile Iron**. International Journal of Metalcasting (IJMC2024), Springer Link, 31 July 2024

EFFECT OF BISMUTH ON MICROSTRUCTURE AND PROPERTIES OF DUCTILE IRON

S. Boonmee, W. Waenthongkham and K. Worakhut
Suranaree University of Technology, Nakhon Ratchasima, Thailand

https://doi.org/10.1007/s40962-024-01421-6

Abstract

This study explores the effect of bismuth on ductile iron to enhance its mechanical properties and to prevent the formation of chunky graphite. Various heats of ductile iron were produced with varying bismuth (0.000–0.010 wt%Bi). Microscopic examinations, Brinell hardness tests, and tension tests were conducted to characterize the samples. The results indicate that Bi influences the microstructure, nodule count, hardness, and tensile strength of the ductile iron, with optimal amount of Bi (0.005–0.007 wt%Bi) depending on section thickness. Bi prevented the carbide formation and increased the nodule count, leading to improved mechanical properties. In addition, the study demonstrated that Ce/Bi values of 1.29–1.60 were corresponding levels that showed optimal microstructure and properties. Thermal analysis demonstrated the inoculation effect of Bi addition by shifting TE_{low} and TE_{high} toward the stable eutectic temperature. Electron Probe Microanalysis (EPMA) results showed that Bi oxide and sulfide were found at the graphite cores as heterogeneous nucleation sites during solidification.

Keywords: *bismuth, Electron Probe Microanalysis, EPMA, chunky graphite, ductile iron, nodule count, graphite fineness, thermal analysis*

Introduction

Ductile iron has been known as one of the most used engineering materials across various industrial applications due to its low production cost, favorable mechanical properties at normal and elevated temperatures. Ductile iron is superior to gray iron in terms of strength and ductility, primarily due to differences in graphite morphology. The nodular graphite present in ductile iron offers reduced stress concentration compared to the lamellar graphite found in gray iron. The typical tensile strength of ductile iron ranges from 400 to 700 MPa, depending on factors such as graphite morphology and matrix structure. Furthermore, the presence of finer graphite contributes to improved mechanical properties. Therefore, the mechanical properties of the ductile iron can be improved by increasing graphite nodularity and nodule count.

The graphite fineness in ductile iron is influenced by various factors, including the cooling rate (e.g. section thickness) and inoculation. Several investigators have explored the impact of Bi on the as-cast microstructure of ductile iron. Takeda et al.[1] found that incorporating 0.005–0.010 wt%Bi increased graphite nodule count (nodules/mm^2). This effect was more pronounced at 2.0 wt%Si compared to higher Si percentages (2.4 and 2.8 wt%Si). The study concluded that Bi reduced chilling tendencies and raised the ferrite ratio in the matrix. Takeda et al.[2] extended their investigations using thermal analysis, showing that the addition of Bi increased the Temperature of Eutectic Start (TES) and Temperature of Eutectic End (TEE). The EPMA findings suggested that metallic Bi, Bi oxide and Bi sulfide particles acted as heterogeneous nuclei, resulting in finer graphite.

In thicker sections, there is a greater tendency for chunky graphite formation. Baer[3] summarized the formation of the chunky graphite that the influencing parameters are chemical composition, melt treatment, section thickness, etc. Chunky graphite is commonly found at the thermal center of the casting section. Although there is no confirmed theory for the formation of the chunky graphite, it is promoted with (i) the presence of excessive rare earth elements; (ii) the higher casting modulus and (iii) the insufficient inoculation. Itofuji et al.[4,5] proposed a theory of the chunky graphite formation through magnesium fading

Received: 28 May 2024 / Accepted: 20 July 2024
Published online: 31 July 2024

and eutectic expansion. Later, Sertucha et al.[6] used the thermal analysis system to explore the growth sequence of the chunky graphite. The sequence involves: (i) nucleation of primary graphite in the liquid; (ii) initial eutectic reaction with growth of austenite dendrites around primary nodules; (iii) bulk eutectic reaction leading to growth of chunky graphite cells and secondary nodules, forming spheroidal graphite eutectic cells. Overall, Stefanescu[7] suggested that the combination of the level of solute and solidification rate is the major factors in graphite nucleation and growth resulting in different graphite morphologies.

The formation of the chunky graphite is detrimental to the mechanical properties of ductile irons. In fact, the chunky graphite is considered as a casting defect that significantly affects the ductility and toughness of ductile iron. Nakayama et al.[8] reported the reduction of tensile strength approximately ~50 MPa for samples with more than 20% chunky graphite. Moreover, the elongation reduced to only 1/5 of the samples without chunky graphite.

Numerous studies[9–15] have investigated the role of Bi in preventing chunky graphite and refining graphite particles. Liang et al.[9] illustrated that adding metallic Bi to the iron melt counteracted the formation of chunky graphite, thereby improving mechanical properties. Additionally, it was concluded that Bi greater than 0.011 wt% did not further enhance mechanical properties, as the excessive Bi addition led to chunky graphite aggregation.

Ferro et al.[10] experimented with the effect of rare earth and Bi in heavy casting section of ductile iron. It was found that chunky graphite formation could be prevented by both rare earth and Bi. In fact, a higher nodule count was observed when Bi was added.

According to Glavas et al.[11], the impact of Bi on ductile iron can be both advantageous and detrimental, depending on the section thickness. In cases of heavier section thickness, Bi was proved beneficial by preventing chunky graphite formation and enhancing nodularity. The study extended to 0.0042 wt%Bi, revealing a consistent upward trend in nodule count for medium and heavy section thickness. However, Bi also increased the chilling tendencies in small section thickness. The results contradicted the findings of an earlier study by Takeda et al.[1] and Horie et al.[12], which suggested that Bi suppressed chilling tendencies. Furthermore, they demonstrated that the nodule count increased with Bi up to 0.005 wt% and then gradually decreased. Similarly, Yicheng et al.[13] conclude that the optimal range of Bi in ductile iron is between 0.004–0.016 wt%Bi for 10 mm and 30–70 mm thickness, respectively. Song et al.[14] reported that Bi improved mechanical properties up to 0.011 wt%Bi. Similarly, Gao et al.[15] performed mechanical testing at − 40 °C and found that the optimal Bi was in the range of 0.010–0.012 wt%Bi for 180 × 180 × 200 mm specimen.

Bauer et al.[16,17] illustrated how Bi prevented the formation of chunky graphite. They demonstrated that the combined influence of the cooling rate and the quantity of cerium determined the optimal amount of Bi. The Ce/Bi ratio was important as higher amounts were associated with adverse effects on mechanical properties. In their experiments, Ce/Bi of 0.6 yielded the best results.

Pan and Chen[18] found that the Ce/Bi ratio of 0.8–1.1 were able to prevent the formation of the chunky graphite in heavy section. They further reported that the Ce/Bi exceeds 1.1 was required for the lighter section.

Stieler et al.[19] further explored the combined effect of Bi and cerium in relation to graphite morphology. Generally, the suitable amount of Bi depends on Ce content and section thickness. The thicker sections requiring higher Bi concentrations than smaller sections.

There have been studies[10,20,21] that experimented with the idea of introducing Bi in inoculants (e.g. Bi-bearing inoculants). Margaria et al.[19] filed a patent for an inoculant product comprising Bi and rare earth. The inoculant contained rare earth, Bi, Sb, and Pb with the ratio (Bi+Pb+Sb/Total RE) between 0.9 and 2.2. Although, there are limitations for comparing between studies. A conclusion can be made that heavier section thickness require more Bi (or lower value of Ce/Bi). Table 1 summarizes the optimal range of Ce/Bi from studies mentioned above.

This study aims to investigate the potential use of Bi as an additive in traditional ductile iron and determine the

Table 1. Summary of the Optimal Ce/Bi from Investigators

Reference	Ce/Bi	Remark
Glavas et al.[11]	0.67	50–100 mm thickness
Bauer et al.[17]	0.60	Up to 300 mm thickness
Pan and Chen[18]	0.80–1.10	Solidification time up to 3200 s
Stieler et al.[19]	1.56–5.30	75 mm thickness
Margaria et al.[20]	0.45–1.11	converted from (Bi+Pb+Sb)/RE

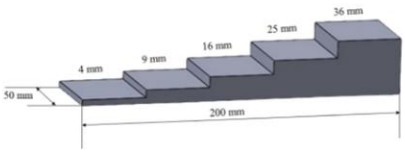

Figure 1. Dimensions of the step casting.

optimal amounts of Bi and Ce/Bi ratio that yield a high nodule count and desirable properties.

Experimental Procedure

Design of Test Castings

There were two types of test castings. The first design was the cylindrical castings for tension test as per ASTM E8. The as-cast diameter was 25.4 mm. The second type of test casting was the step casting. It was designed to accommodate the study of the effect of cooling rates. Figure 1 depicts the basic dimensions of the step casting, featuring various thicknesses from 4 to 36 mm. A commercial casting simulation software was used to estimate the corresponding cooling rates of section thicknesses. Furthermore, the cooling curves were retrieved from virtual thermocouples inserted at the geometrical center of each section. Figure 2 shows the simulated cooling rates and cooling curves. Overall, the simulated cooling rates were approximately in the range of 1.0–18.0 °C/sec. These cooling rates were taken at 5 °C above eutectic temperature. Noted that the latent heat release was dictated by the heat of formation and enthalpy provided by the software database. The enthalpy was a function of temperature. The local solidification times ranged from a few seconds to several minutes representing typical section thicknesses in the industrial applications.

Production of the Test Castings

Five batches of ductile iron were produced using a 100-kg induction furnace, each with different Bi levels (ranging from 0 to 0.01 wt% Bi). Throughout the experiment, carbon, Si, and manganese remained constant. After cleaning, the melt was superheated to eliminated existing nuclei at 1500 °C and tapped at approximately at 1450 °C, respectively. Metallic Bi was added to the melt before tapping. Spheroidization was done using rare earth-containing FeSiMg (Fe-45Si-5.2Mg-2.0Ca-0.4Al-2.23RE). The base melt for the spheroidization was 100 kg of iron melt. Inoculation (Fe-75Si, 0.2% by weight of the melt) took

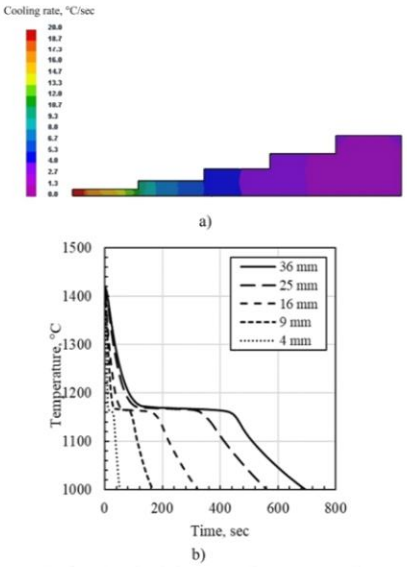

Figure 2. Result of casting simulation; (a) cooling rate; (b) cooling curves.

Table 2. Experimental Parameters for the EPMA Experiment

	Parameter
Acceleration voltage	15 kV
Beam size	1 μm
Current	7.5 nA
Measuring time	10 msec
Step size	0.4 μm
Total area size	410 × 307 μm

place before pouring at around 1380 °C. Green sand molds were used for casting, with two types of test casting: step casting and cylindrical casting. Silica sand with the Grain Fineness Number (GFN) was between 55 and 60. The chemical compositions were taken from the Optical Emission Spectrometry (OES) and amount of Bi and Ce were determined by Inductively Coupled Plasma Optical Emission Spectrometry (ICP-OES).

Table 3. The Chemical Composition of the Ductile Irons in This Study

Heat	Composition, wt%									
	Bi	C	Si	Mn	P	S	Mg	CE	Ce	Ce/Bi
1	0.0001	3.41	2.59	0.064	0.037	0.01	0.078	4.27	0.007	70.0
2	0.003	3.42	2.45	0.061	0.041	0.01	0.088	4.24	0.008	2.67
3	0.005	3.40	2.57	0.064	0.040	0.01	0.079	4.26	0.008	1.60
4	0.007	3.41	2.46	0.055	0.046	0.03	0.077	4.23	0.009	1.29
5	0.010	3.47	2.47	0.058	0.044	0.01	0.078	4.29	0.010	1.00

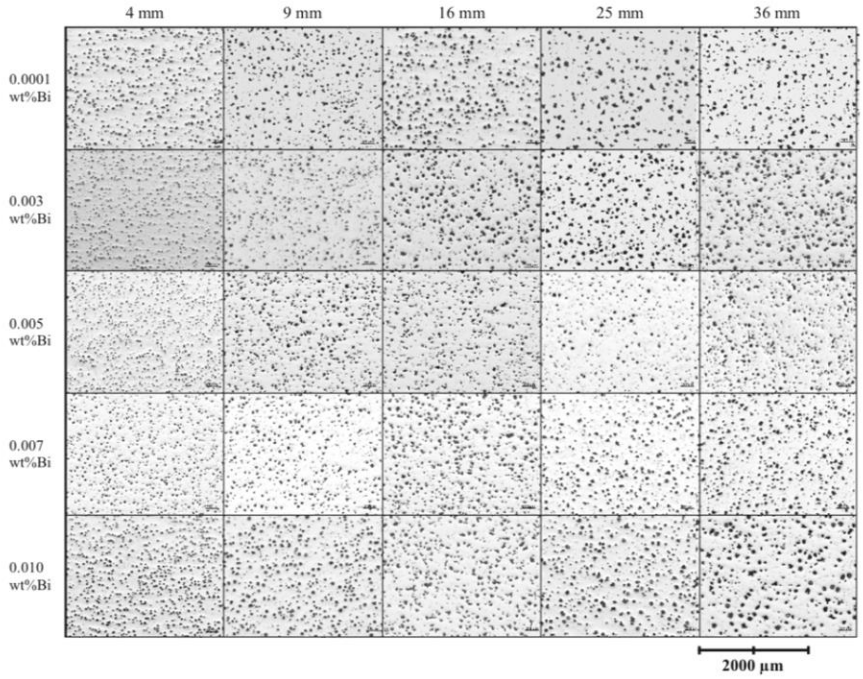

Figure 3. Microstructure of ductile irons with various section thickness and Bi (unetched).

Characterization

Microscopic examinations were conducted at the geometrical centers of each step, and Brinell hardness tests were performed at corresponding locations. The cylindrical castings had a diameter of 25.4 mm, which were later machined to 20 mm diameter and tested according to ASTM E8 standards. Cooling curves were obtained for all

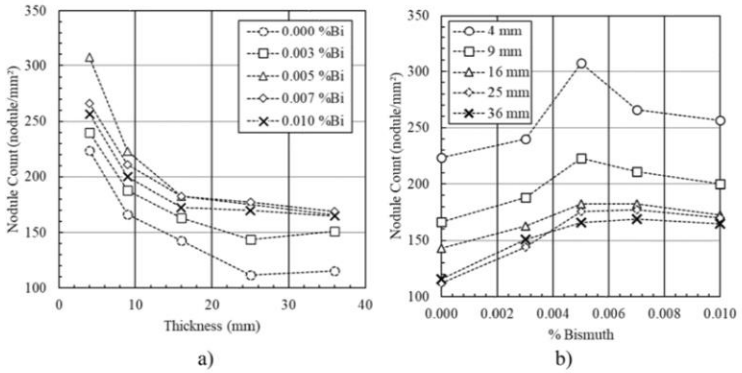

Figure 4. Effect of Bi and section thickness on nodule count; (a) section thickness; (b) Bi.

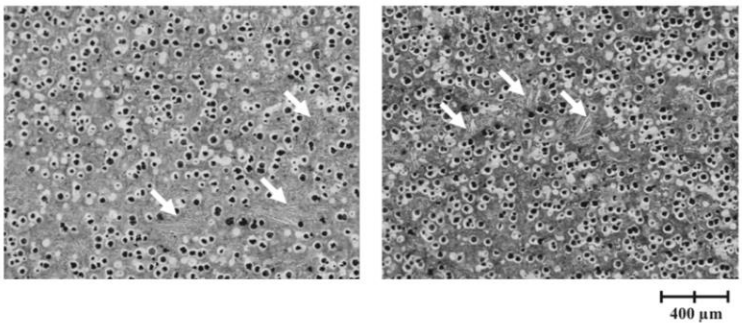

Figure 5. Carbide found in sample with 4-mm section thickness; (left) 0.000 wt%Bi (right) 0.003 wt%Bi.

batches through thermal analysis cups with a diameter of 31 mm and a height of 53 mm.

For microstructure analysis, the unetched micrographs were used for measuring nodule counts with an image analysis software. Particles smaller than 1 μm^2 were excluded from the analyzes as they were likely artifacts from sample preparation. Circularity was also analyzed for all samples. The definition of Circularity is given by Eqn. 1.

$$C = 4\pi A/P^2 \qquad \text{Eqn. 1}$$

where A and P are the area and perimeter of graphite particles, respectively.

The image analysis was conducted for the etched micrographs to quantify the constituents of the graphite, pearlite, ferrite and carbide. The images used were taken at 100×

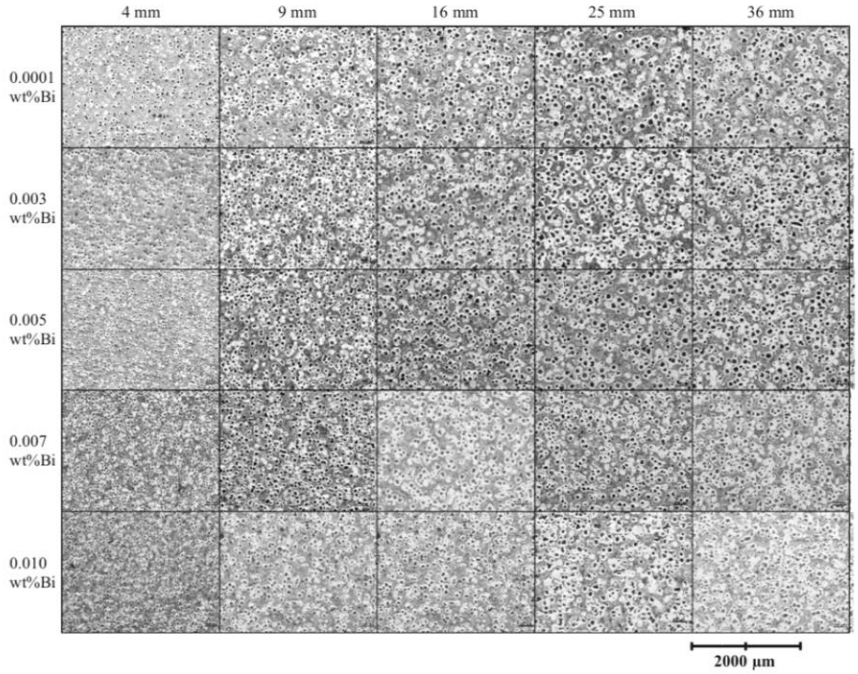

Figure 6. Microstructure of ductile irons with various section thickness and Bi (etched, 3%Nital).

magnification at the middle of each section thickness. At least 5 images were used for one condition of the analysis. The graphite or phases that were cropped by the edge of the image were excluded from the analysis. The image size was 2560 × 1920 pixels (~ 4.9 megapixels). The image resolution was kept constant throughout the process.

Color metallography was applied to selected samples, and the etchant used was 80 g NaOH, 20 g KOH, 20 g picric acid in 200 ml distilled water. The samples were immersed in the etchant at 120 °C for 120 seconds.

The Electron Probe Micro Analysis (EPMA) was conducted on a selected sample to observe the elemental distribution in the microstructure. Table 2 shows the criteria used in the EPMA experiment.

Results and Discussion

Chemical Composition

Table 3 presents the chemical composition of the iron produced in this study. The levels of C, Si, Mn, P and S were maintained within a narrow range. The Carbon Equivalents (CE = %C + 1/3(%Si+%P)) indicated that all conditions approached eutectic compositions. The Mg level exceeded typical industry values, to assess the impact of rare earth in thicker sections and its combined influence with Bi. Higher Mg can lead the carbide formation as magnesium increases the chilling tendency. In addition, the FeSiMg that was used as the source of Mg also contains cerium that interplays with Bi. Bi content ranged from 0 to 0.01 wt%Bi, with some losses during addition to the melts.

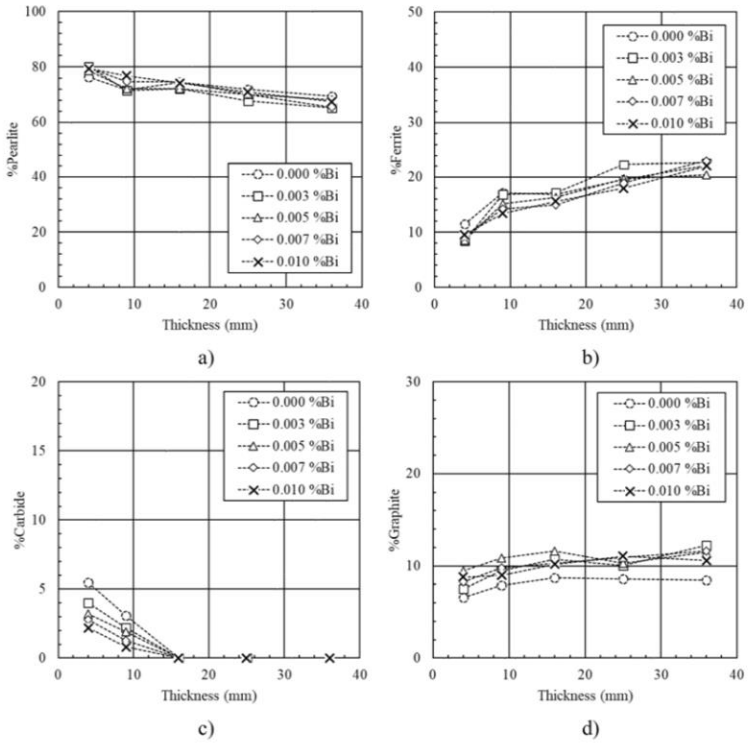

Figure 7. Percentage area of phases in microstructure as a function of section thickness; (a) pearlite; (b) ferrite; (c) carbide; (d) graphite.

Additionally, Al and Sn were present at levels of 0.009 wt%Al and 0.0024 wt%Sn, respectively, their effects were not observable in the experiment, no spiky graphite was found throughout the experiment. Other elements were present in trace amounts (<0.0004 wt%As, <0.0005 wt%Pb, <0.0004 wt%Sb, <0.00001 %wtCd, <0.00003 wt%La). The rare earth element used in this experiment was primarily Ce. Because La, Pb and Sb were at a very low levels, therefore; the ratio of Ce/Bi is presented in Table 1 for further analysis.

Microstructure

Figure 3 illustrates the microstructure of unetched samples with varying thickness and Bi. Overall, the Circularity exceeded 0.8, indicating acceptable nodularity across all samples, even in the case of the thickest section. Figure 4a shows the effect of section thickness on nodule count. It is seen that the thicker sections resulted in lower nodule counts due to the slow cooling rate. The measured nodule count was comparable to the findings in Reference 12 and 13. Figure 4b shows the influence of Bi on nodule count. For 4-mm and 9-mm section thickness, the nodule count

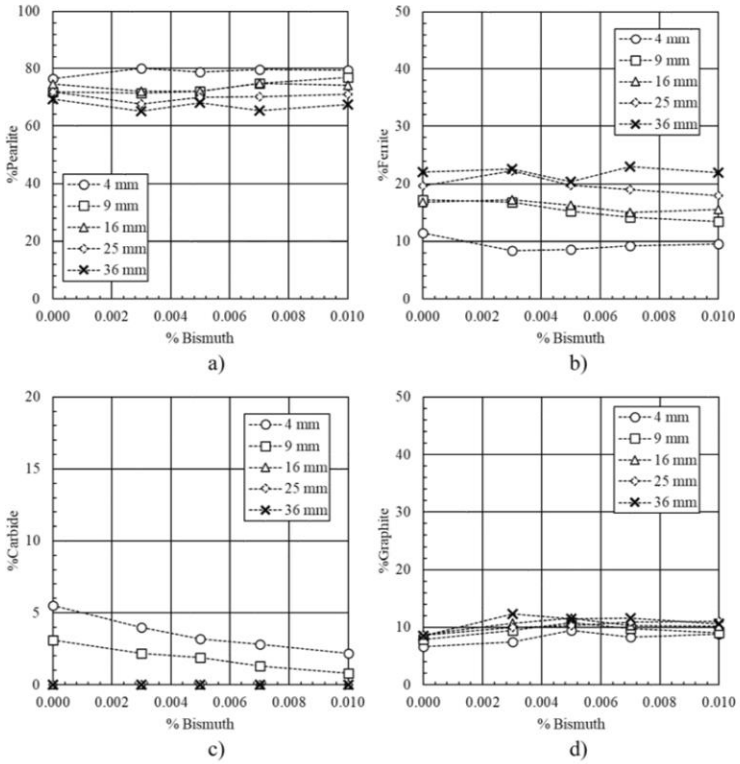

Figure 8. Percentage area of phases in microstructure as a function of %Bi; (a) pearlite; (b) ferrite; (c) carbide; (d) graphite.

increased with Bi up to 0.005 wt%Bi. At higher Bi, the nodule counts decreased. For 16-, 25-, and 36-mm section thickness, the nodule count peaked at 0.007 wt%Bi and there was no clear decreasing trend in nodule count at higher Bi. This suggests that heavier section thickness requires a higher Bi concentration for graphite refinement. The mechanism behind the effect of Bi on nodule count will be discussed later. It is worth noting that samples with 4-mm section thickness without Bi displayed carbide formation in the microstructure, due to the high cooling rate and Mg content. In fact, Mg, known for promoting chill formation, was relatively high in this study. Figure 5 illustrates carbide formation in samples with 4-mm section thickness. The carbide formation reduced the amount of graphite, a very low nodule count was observed at 4-mm section thickness. However, this effect gradually disappeared at thicker section and higher Bi. In this study, the effect of Bi in decreasing the chilling tendency was observed similarly to previously reported in Reference 12, 13 and 17.

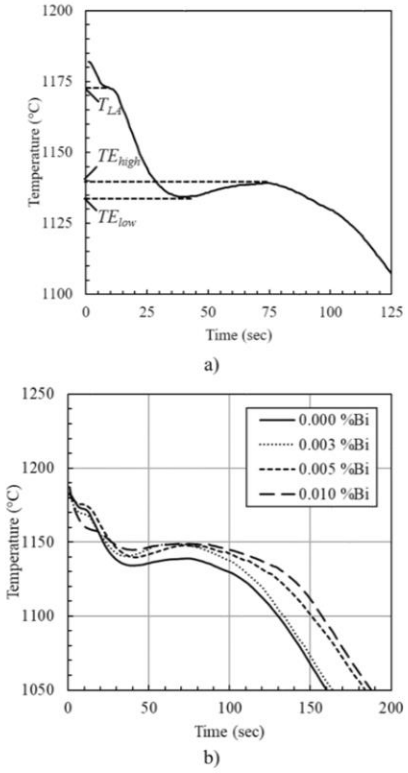

Figure 9. Cooling curves; (a) definitions of symbol; (b) from ductile iron samples with 0–0.010 wt%Bi.

Figure 6 shows the microstructure of etched samples. Figure 7 displays the image analysis results of the etched samples showing the percentage of phases in the microstructure. Overall, pearlite was the dominant phase in the matrix structure (Figure 7a). The percentage of ferrite increased with increasing thickness due to the slower cooling rate (Figure 7b). The carbide appeared in all 4 and 9-mm samples and completely disappeared at 16 mm and thicker (Figure 7c). Consequently, the percentage of graphite in 4-mm and 9-mm were lower than the rest due to the carbide formation (Figure 7d).

Table 4. Summary of Characteristic Temperatures Retrieved From Cooling Curves

Heat	Bi	CE	Ce/Bi	T_{LA}	TE_{low}	TE_{high}
1	0.0001	4.27	180	1175	1133	1140
2	0.003	4.24	7.33	1171	1139	1148
3	0.005	4.26	3.20	1176	1140	1149
4	0.007	4.23	2.57	1173	1134	1148
5	0.010	4.29	1.60	1159	1143	1149

The effect of Bi on the microstructure is shown in Figure 8. There was no clear trend on the percentage pearlite and ferrite (Figure 8a and b). Similar results were reported by Yicheng et al.[13]. The effect of Bi was more pronounced in Figure 8c. The percentage carbide clearly decreased with the increasing Bi. This confirms the effect of Bi on carbide suppression at thinner sections reported by Takeda et al.[1] and Horie et al.[12]

Figure 9 displays the cooling curves during the eutectic reaction for samples containing 0.00 to 0.01 wt%Bi. It is important to note that these curves were obtained from thermal analysis cups, not directly from the step castings. The thermal analysis cups have a casting modulus of approximately 0.98 cm. Table 4 summarizes the Temperature of Liquidus Arrest (T_{LA}), The Lower Temperature of Eutectic (TE_{low}) and the Higher Temperature of Eutectic (TE_{high}). It is clearly seen that the presence of Bi increased TE_{low} and TE_{high}, shifting TE_{low} from 1133 to 1143 °C and TE_{high} from 1140 to 1149 °C for 0 and 0.01 wt%Bi, respectively. The increased TE_{low} and TE_{high} were caused by the inoculation effect of Bi addition. It should be noted that this effect can be observed by the analysis of the cooling curves.

Figure 10 illustrates the effect of Bi and section thickness on hardness. The hardness of the fully ferritic (ASTM A536 Grade 60-40-18) and fully pearlitic (ASTM A536 Grade 100-70-03) ductile irons are 143–187 and 240–300 BHN, respectively.[21] Overall, the hardness values in this experiment were in the typical range for the pearlito-ferrite ductile iron. A noticeable trend is observed where hardness decreased with increasing section thickness due to the slower cooling rate resulting in lower nodule count and greater ferrite in the matrix. It is worth noting that carbide formation, observed in all 4-mm section thickness samples,

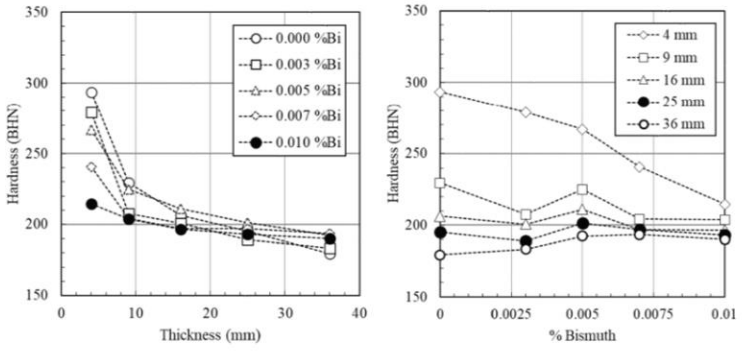

Figure 10. Effect of Bi and section thickness on hardness; (a) thickness; (b) Bi.

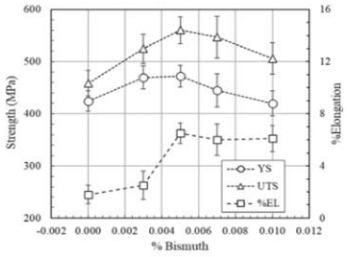

Figure 11. Mechanical properties of ductile iron with 0–0.01 wt%Bi; Yield strength (YS), Ultimate Tensile Strength (UTS) and Percent Elongation (%EL).

contributes to increased hardness, the effect reflected in Figure 10b. As seen, the initial hardness of 4-mm section thickness without Bi was significantly high, and increasing of Bi to 0.003 wt% decreased hardness. The hardness of the samples with 4-mm section thickness was high due to the carbide formation. A similar effect of carbide formation on hardness is seen in 9- and 16-mm section thickness but in lesser degree. At thicker section, hardness increases with Bi, peaking at 0.005–0.007 wt%Bi. Higher Bi concentrations are more favorable for achieving increased hardness in thicker section. In addition, hardness decreased with the increasing section thickness due to slower cooling and higher ferrite/pearlite ratio at the same level of Bi shown in Figure 7.

In Figure 11, the influence of Bi on ultimate tensile strength, yield strength and percent elongation is presented. The trend indicates that lower Bi concentrations resulted in lower strength and elongation, due to the lower nodule count and carbide formation. Elongation improved significantly beyond 0.005 wt%Bi due to the suppression of carbide formation. In fact, 0.005 wt%Bi samples demonstrated the highest strength in this study. It is important to note that the tensile samples have a casting modulus of 6.35 mm close to a 16-mm section thickness, aligning the observed behavior with the hardness trends depicted in Figure 10.

In summary, the optimal Bi content was contingent on the section thickness. For sections with thicknesses of 4, 9, and 16 mm, 0.005 wt%Bi (Ce/Bi = 1.60) exhibited the best outcomes in terms of nodule count, hardness, and tensile strength. However, for sections with thicknesses of 25 and 36 mm, 0.007 wt%Bi (Ce/Bi = 1.29) demonstrated better results. It is worth noting that if there were variations in cerium (Ce), the determination of the optimal Bi content needs to be guided by the Ce/Bi ratio. The findings suggest that Bi is more advantageous as section thickness increases by preventing the formation of chunky graphite and refining graphite particles. When comparing the optimal Ce/Bi ratio to Table 1, it is seen that the optimal Ce/Si ratio in this study is higher than the table suggests. This is due to the

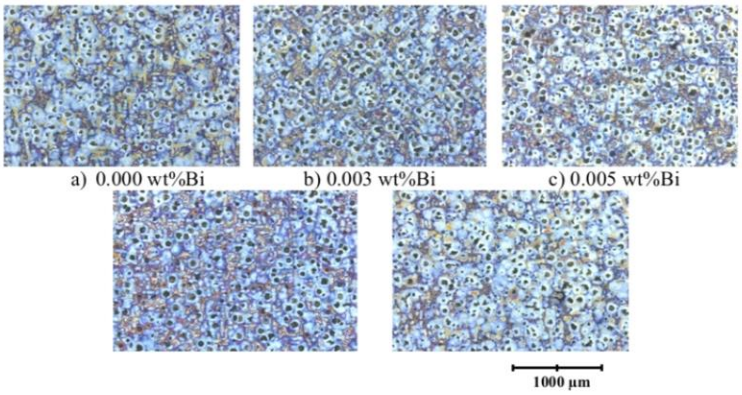

Figure 12. Color-etch micrographs of ductile irons with 0–0.010 wt%Bi at 36-mm section thickness.

small section thickness in this study. Pan and Chen[16] also mentioned that the optimal Ce/Bi ratio for lighter sections would have been more than 1.1.

Figure 12 shows color-etched micrographs of ductile irons with 0–0.01 wt%Bi at a section thickness of 36 mm. The color metallography revealed the microsegregation of elements, primarily Si and Mn, within the microstructure. This enables the observation of the dendritic structure and the impact of Bi on dendrite arm spacing. However, no significant difference in dendrite arm spacing was observed with varying Bi.

Figure 13 shows the EPMA results of a sample with 0.010 wt%Bi and 36-mm section thickness. The testing field was selected to have several graphite particles along with interparticle area to observe the microsegregation of elements. The microstructure showed low nodularity due to the slower cooling rate and higher Bi. Figure 13a and b shows the ferrite, pearlite pattern and location of graphite particles in the microstructure which aligns with the carbon mapping (Figure 13c). The Si mapping in Figure 13d shows that Si tended to be more in the matrix around graphite and less in the interparticle area. Mg, S, O and Bi were found in the same area indicating the formation of intermetallic compound between them. Ce showed a similar pattern with weaker signal.

To discuss the microsegregation of Bi, the superimposed image between the carbon and Bi is created (Figure 14). As seen, Bi tends to reside at the center of graphite particles. This indicates that Bi is involved with the nucleation of graphite. Moreover, O and S are also found in the graphite cores where Bi is presented.

Figure 15 shows the EPMA mapping of Bi, oxygen and sulfur at the graphite cores which suggests that the nucleation sites are made up of these elements in form of compounds such as Bi oxide and sulfide. This finding is inline with the results by Takeda et al.[2] and Horie et al.[12]. The mechanism for graphite refining by Bi addition is proposed as follows:

- Bi presents itself as a small droplet in iron melt. This is because Fe and Bi form a monotectic reaction. According the Bi-Fe phase diagram (Figure 16), it is seen that the monotectic reaction is $L_2 = L_1 + \delta$ ferrite. The two types of liquid have very limited solubility. Therefore, it is possible to have Bi-rich droplets dispersed in iron melt. The

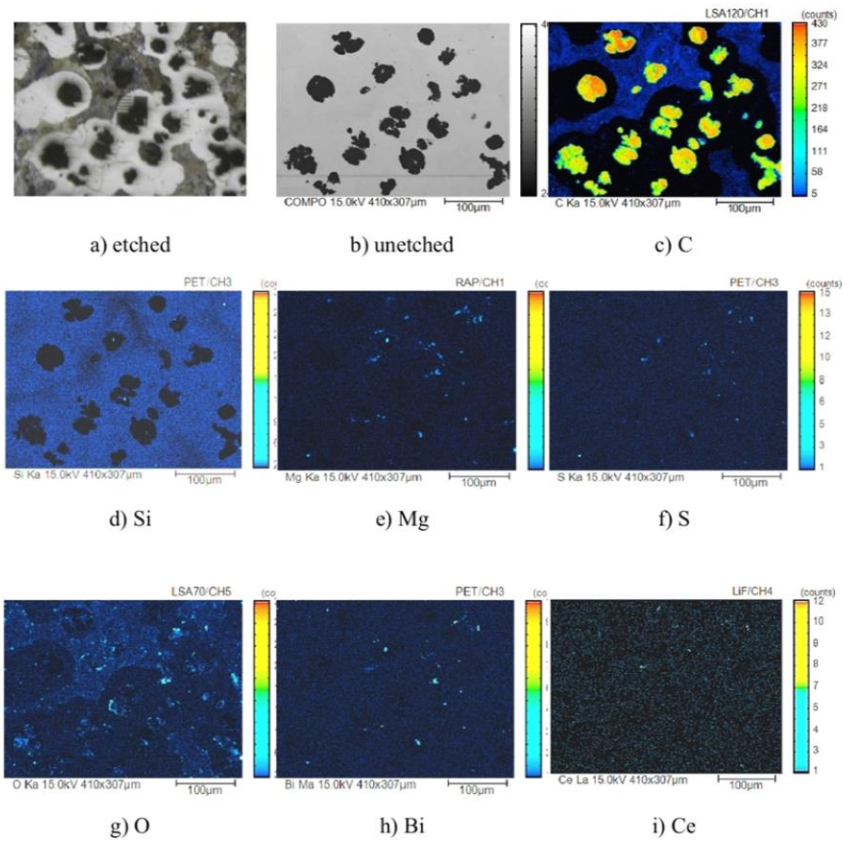

Figure 13. Microstructure and EPMA mappings of the sample with 0.010 wt%Bi and 36-mm section thickness.

Bi-rich droplets presumably exist in the melt down to the monotectic temperature.

- During solidification, Bi-rich droplets precipitate and become oxide and sulfide by combining with O and S available in the melt. Table 5 shows the physical properties of Bi and related compounds. It is seen that Bi oxide (Bi_2O_3) and Bi sulfide (Bi_2S_3) have negative standard free energy of formation at 1500 °C, indicating spontaneous formation of these compounds. These compounds later become heterogeneous nucleation sites for graphite.
- During the spheriodization, Mg is introduced to the melts and can then react with the existing

Bi_2O_3 and Bi_2S_3 forming more stable compounds such as magnesium oxide (MgO) and sulfide (MgS). This is supported by the presence of magnesium in the same area to Bi, oxygen and sulfur in the EPMA mappings. Si can also be involved by forming magnesium silicide. The result of this process is the reduction of Bi compounds to metallic Bi at the graphite cores. Therefore, it is possible to find the coexistence of Bi_2O_3, Bi_2S_3, MgO, MgS, and Mg_2Si.

Conclusions

This work investigates the influence of Bi on microstructure and mechanical properties of ductile iron. The results showed that the presence of appropriate levels of Bi in ductile iron leads to improvements in microstructure and properties.

- The addition of 0.005–0.007 wt%Bi resulted in a refined microstructure, with a higher nodule count. The further addition of Bi reduced the nodule count and had adverse effects on mechanical properties.
- The refined microstructure increased the strength and hardness of the ductile iron with casting section thickness 9–36 mm. The improvement of the tensile strength and yield strength was approximately 20% at 0.005 wt%Bi addition. At smaller section thicknesses (for example, 4 mm), chill was observed in all samples. Moreover, the results showed that the addition of Bi suppressed the formation of carbides.
- The ratio of Ce/Bi can be used as a guide for the required Bi addition depending on the section thickness. The lighter section thickness requires a higher Ce/Bi ratio. In this study, the optimal Ce/Bi

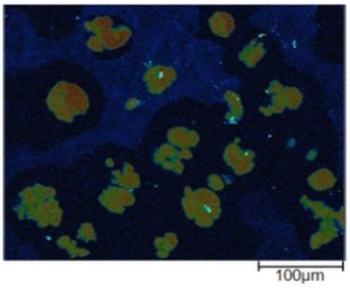

Figure 14. Combined image of carbon and Bi EPMA mapping.

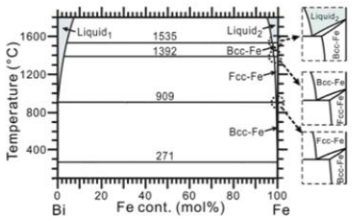

Figure 16. Bi–Fe phase diagram[22].

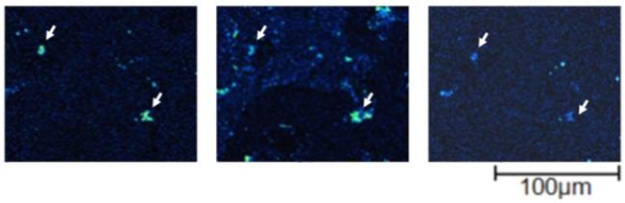

Figure 15. EPMA mapping of Bi, O and S at the graphite cores.

Table 5. Physical Properties and Standard Free Energy of Formation of Related Compounds

Compound	Melting point, °C	Boiling point, °C	Density, g/cm^3	Standard free energy of formation at 1500 °C, kJ/mol[2]	References
Bi	271	1564	9.79	–	23
Bi_2O_3	817	1890	8.90	− 136.5*	24
Bi_2S_3	850	–	6.78	− 64.35	25
MgO	2852	3600	3.60	− 733.7	26
MgS	2000	–	2.84	− 395.2	27

*ΔG_f°, Bi_2O_3 = − 584235 + 289.28(T/K) [28]

ratios were 1.60 for 4–16 mm section thickness and 1.29 for 25–36 mm section thicknesses.

- The introduction of Bi shifted the cooling curves toward stable eutectic solidification resulting in reduction of chilling tendency and higher nodule count. This can be observed by the increase in TE_{low} and TE_{high} using thermal analysis.
- The EPMA results suggested that Bi form oxide and sulfide that act as heterogeneous nucleation sites during solidification.

Acknowledgement

This work was supported by the SUT Research and Development Fund, Suranaree University of Technology, Thailand.

REFERENCES

1. H. Takeda, K. Asano, H. Yoneda, Effect of bismuth on refinement of graphite in thin wall spheroidal graphite cast iron. Int. J. Cast Met. Res. **21**(1–4), 81–85 (2008). https://doi.org/10.1179/136404608X361710
2. H. Takeda, H. Yoneda, K. Asano, Effect of silicon and bismuth on solidification structure of thin wall spheroidal graphite cast iron. Mater. Trans. **51**, 176–185 (2010). https://doi.org/10.2320/matertrans.M2009255
3. W. Baer, Chunky graphite in ferritic spheroidal graphite cast iron: formation, prevention, characterization, impact on properties: an overview. Inter. Metalcast. **14**, 454–488 (2020). https://doi.org/10.1007/s40962-019-00363-8
4. H. Itofuji, H. Uchikawa, Formation mechanism of chunky graphite in heavy-section ductile cast irons. Trans. AFS **98**, 429–448 (1990)
5. H. Itofuji, A. Masutani, Nucleation and growth behaviour of chunky graphite. Int. J. Cast Met. Res. **14**(1), 1–14 (2001). https://doi.org/10.1080/13640461.2001.11819419
6. J. Sertucha, R. Suarez, I. Asenjo, P. Larranaga, J. Lacaze, I. Ferrer, S. Armendariz, Thermal analysis of the formation of chunky graphite during solidification of heavy-section spheroidal graphite iron parts. ISIJ Int. **49**(2), 220–228 (2009). https://doi.org/10.2355/isijinternational.49.220
7. D.M. Stefanescu, Solidification and modeling of cast iron—A short history of the defining moments. Mater. Sci. Eng. A **413–414**, 322–333 (2005). https://doi.org/10.1016/j.msea.2005.08.180
8. H. Nakayama, B.-R. Zhao, N. Furusato, S. Yamada, T. Nishi, H. Ohta, Effect of amount of chunky graphite on mechanical properties of spheroidal graphite cast iron. Mater. Trans. **59**(3), 412–419 (2018). https://doi.org/10.2320/matertrans.M2017305
9. S. Liang, G. Erjun, T. Chang-long, Effect of Bi on graphite morphology and mechanical properties of heavy section ductile cast iron. China Foundry **11**, 125–131 (2014)
10. P. Ferro, A. Fabrizi, R. Cervo, C. Carollo, Effect of inoculant containing rare earth metals and bismuth on microstructure and mechanical properties of heavy-section near-eutectic ductile iron castings. J. Mater. Process. Technol. **213**, 1601–1608 (2013). https://doi.org/10.1016/j.jmatprotec.2013.03.012
11. Z. Glavas, A. Strkalj, K. Maldini, F. Kozina, Effect of bismuth and rare earth elements on graphite structure in different section thicknesses of spheroidal graphite cast iron castings. Arch. Metall. Mater. **63**, 1547–1553 (2018)
12. H. Horie, T. Kowata, A. Chida, Influence of bismuth on graphite nodule count in thin-section spheroidal-graphite cast irons. Int. J. Cast Met. Res. **2**, 197–202 (1989)
13. F. Yicheng, M. Mengdi, W. Changliang et al., Effect of trace element Bi on microstructure and mechanical properties of ductile cast iron with different wall thickness. Trans. Indian Inst. Met. **76**, 2669–2679 (2023). https://doi.org/10.1007/s12666-022-02856-3
14. W.L. Gao, G. Cen, Z.C. Yan, X.F. Song, Effect of Bi on the microstructure and mechanical properties of heavy section ductile cast iron. J. Hunan Univ. Nat. Sci. **40**(6), 74–79 (2013)
15. L. Song, E. Guo, C. Tan, Effect of Bi on graphite morphology and mechanical properties of heavy section ductile cast iron. China Foundry **11**(2),

125–131 (2014). https://doi.org/10.3969/j.issn.1672-6421.2014.02.009
16. B. Bauer, I. Mihalic Pokopec, M. Petrič et al., Effect of bismuth on preventing chunky graphite in high-silicon ductile iron castings. Inter. Metalcast. **14**, 1052–1062 (2020). https://doi.org/10.1007/s40962-020-00419-0
17. B. Bauer, I. Mihalic Pokopec, P. Mrvar et al., Influence of chemical composition and cooling rate on chunky graphite formation in thick-walled ductile iron castings. Inter Metalcast **17**, 2050–2061 (2023). https://doi.org/10.1007/s40962-022-00913-7
18. E.N. Pan, C.Y. Chen, Effects of Bi and Sb on graphite structure of heavy-section ductile cast iron. AFS Trans. **104**, 845–858 (1996)
19. F. Stieler, D. Funk, B. Tonn, Alteration of the graphite morphology in solid solution-strengthened ductile iron due to high contents of cerium and bismuth. Inter Metalcast **17**, 1315–1325 (2023). https://doi.org/10.1007/s40962-022-00857-y
20. T. Margaria, R. Siclari, Inoculant products comprising bismuth and rare earth (U.S. Patent No. 7,569,092 B2). U.S. Patent and Trademark Office, (2009)
21. Standard Specification for Ductile Iron Castings. (ASTM International, 2019)
22. A. Kishimoto, T. Uda, Thermodynamics on the Bi-Fe-Ti system and the gibbs energy of Bi9Ti8. Metall. Mater. Trans. B **49**, 2975–2985 (2018). https://doi.org/10.1007/s11663-018-1393-6
23. J.W. Arblaster, Selected Values of the Crystallographic Properties of Elements. Materials Park, Ohio, (ASM International, 2008)
24. P. Patnaik, *Handbook of inorganic chemical compounds* (McGraw-Hill, New York, 2003), p.243
25. N. Greenwood, A. Earnshaw, *Chemistry of the elements*, 2nd edn. (Butterworth-Heinemann, Oxford, 1997), pp.85–66
26. W.M. Haynes, *CRC handbook of chemistry and physics*, 92nd edn. (CRC Press, Boca Raton, 2011), pp.4–74
27. C. Bradford, C.B. O'Donnell, B. Urbaszek, A. Balocchi, C. Morhain, K.A. Prior, B.C. Cavenett, Growth of zinc blende MgS/ZnSe single quantum wells by molecular-beam epitaxy using ZnS as a sulphur source. Appl. Phys. Lett. **76**(26), 3929–3921 (2000). https://doi.org/10.1063/1.126824
28. K.T. Jacob, A.K. Mansoor, Gibbs energy of formation of bismuth (III) oxide. Thermochimica Acta **630**, 90–96 (2016). https://doi.org/10.1016/j.tca.2016.02.006